



AGN STORM 2. VIII. Investigating the Narrow Absorption Lines in Mrk 817 Using HST-COS Observations*

Maryam Dehghanian¹ , Nahum Arav¹ , Gerard A. Kriss² , Missagh Mehdipour² , Doyee Byun¹ , Gwen Walker¹ ,
Mayank Sharma¹ , Aaron J. Barth³ , Misty C. Bentz⁴ , Benjamin D. Boizelle⁵ , Michael S. Brotherton⁶ ,
Edward M. Cackett⁷ , Elena Dalla Bontà^{8,9,10} , Gisella De Rosa² , Gary J. Ferland¹¹ , Carina Fian¹² ,
Alexei V. Filippenko¹³ , Jonathan Gelbord¹⁴ , Michael R. Goad¹⁵ , Keith Horne¹⁶ , Yasaman Homayouni^{2,17,18} ,
Dragana Ilic^{19,20} , Michael D. Joner²¹ , Erin A. Kara²² , Shai Kaspi²³ , Christopher S. Kochanek^{24,25} , Kirk T. Korista²⁶ ,
Peter Kosec^{22,27} , Andjelka B. Kovačević¹⁹ , Hermine Landt²⁸ , Collin Lewin²⁹ , Ethan R. Partington³⁰ ,
Luka Č. Popović^{19,31} , Daniel Proga³² , Daniele Rogantini²² , Matthew R. Siebert³³ , Thaisa Storchi-Bergmann³⁴ ,
Marianne Vestergaard^{35,36} , Timothy. Waters³⁷ , Jian-Min Wang^{38,39,40} , Fatima Zaidouni²² , and Ying Zu^{41,42,43}

¹ Department of Physics, Virginia Tech, Blacksburg, VA 24061, USA

² Space Telescope Science Institute, 3700 San Martin Drive, Baltimore, MD 21218, USA

³ Department of Physics and Astronomy, 4129 Frederick Reines Hall, University of California, Irvine, CA 92697-4575, USA

⁴ Department of Physics and Astronomy, Georgia State University, 25 Park Place, Suite 605, Atlanta, GA 30303, USA

⁵ Department of Physics and Astronomy, N284 ESC, Brigham Young University, Provo, UT 84602, USA

⁶ Department of Physics and Astronomy, University of Wyoming, Laramie, WY 82071, USA

⁷ Department of Physics and Astronomy, Wayne State University, 666 W. Hancock Street, Detroit, MI 48201, USA

⁸ Dipartimento di Fisica e Astronomia “G. Galilei,” Università di Padova, Vicolo dell’Osservatorio 3, I-35122 Padova, Italy

⁹ INAF-Osservatorio Astronomico di Padova, Vicolo dell’Osservatorio 5 I-35122, Padova, Italy

¹⁰ Jeremiah Horrocks Institute, University of Central Lancashire, Preston, PR1 2HE, UK

¹¹ Department of Physics and Astronomy, The University of Kentucky, Lexington, KY 40506, USA

¹² Departamento de Astronomía y Astrofísica, Universidad de Valencia, E-46100 Burjassot, Valencia, Spain

¹³ Department of Physics and Astronomy, University of California, Berkeley, CA 94720-3411, USA

¹⁴ Spectral Sciences Inc. 30 Fourth Avenue, Suite 2 Burlington, MA 01803, USA

¹⁵ School of Physics and Astronomy, University of Leicester, University Road, Leicester, LE1 7RH, UK

¹⁶ SUPA School of Physics and Astronomy, North Haugh, St. Andrews, KY16 9SS, Scotland, UK

¹⁷ Department of Astronomy and Astrophysics, The Pennsylvania State University, 525 Davey Laboratory, University Park, PA 16802, USA

¹⁸ Institute for Gravitation and the Cosmos, The Pennsylvania State University, University Park, PA 16802, USA

¹⁹ University of Belgrade—Faculty of Mathematics, Department of Astronomy, Studentski trg 16, 11000 Belgrade, Serbia

²⁰ Hamburger Sternwarte, Universität Hamburg, Gojenbergsweg 112, 21029 Hamburg, Germany

²¹ Department of Physics and Astronomy, N283 ESC, Brigham Young University, Provo, UT 84602, USA

²² MIT Kavli Institute for Astrophysics and Space Research, Massachusetts Institute of Technology, Cambridge, MA 02139, USA

²³ School of Physics and Astronomy and Wise Observatory, Tel Aviv University, Tel Aviv 69978, Israel

²⁴ Department of Astronomy, The Ohio State University, 140 W. 18th Avenue, Columbus, OH 43210, USA

²⁵ Center for Cosmology and AstroParticle Physics, The Ohio State University, 191 West Woodruff Avenue, Columbus, OH 43210, USA

²⁶ Department of Physics, Western Michigan University, 1120 Everett Tower, Kalamazoo, MI 49008-5252, USA

²⁷ Center for Astrophysics—Harvard & Smithsonian, Cambridge, MA, USA

²⁸ Centre for Extragalactic Astronomy, Department of Physics, Durham University, South Road, Durham DH1 3LE, UK

²⁹ MIT Kavli Institute for Astrophysics and Space Research, MIT, 77 Massachusetts Avenue, Cambridge, MA 02139, USA

³⁰ Department of Physics and Astronomy, Wayne State University, 666W. Hancock Street, Detroit, MI 48201, USA

³¹ Astronomical Observatory Belgrade, Volgina 7, 11000 Belgrade, Serbia

³² Department of Physics & Astronomy, University of Nevada, Las Vegas 4505 S. Maryland Parkway, Las Vegas, NV 89154-4002, USA

³³ Space Telescope Science Institute, 3700 San Martin Drive, Baltimore, MD 21218-2410, USA

³⁴ Departamento de Astronomia—IF, Universidade Federal do Rio Grande do Sul, CP 15051, 91501-970 Porto Alegre, RS, Brazil

³⁵ Steward Observatory, University of Arizona, 933 North Cherry Avenue, Tucson, AZ 85721, USA

³⁶ DARK, The Niels Bohr Institute, University of Copenhagen, Jagtvej 155, DK-2200 Copenhagen, Denmark

³⁷ X-Computational Physics Division, Los Alamos National Laboratory, NM 87545, USA

³⁸ Key Laboratory for Particle Astrophysics, Institute of High Energy Physics, Chinese Academy of Sciences, 19B Yuquan Road, Beijing 100049, People’s Republic of China

³⁹ School of Astronomy and Space Sciences, University of Chinese Academy of Sciences, 19A Yuquan Road, Beijing 100049, People’s Republic of China

⁴⁰ National Astronomical Observatories of China, 20A Datun Road, Beijing 100020, People’s Republic of China

⁴¹ Tsung-Dao Lee Institute, Shanghai Jiao Tong University, Shanghai 200240, People’s Republic of China

⁴² Department of Astronomy, School of Physics and Astronomy, Shanghai Jiao Tong University, 800 Dongchuan Road, Shanghai, 200240, People’s Republic of China

⁴³ Shanghai Key Laboratory for Particle Physics and Cosmology, Shanghai Jiao Tong University, Shanghai 200240, People’s Republic of China

Received 2024 April 4; revised 2024 July 1; accepted 2024 July 3; published 2024 September 3

* Based on observations made with the NASA/ESA Hubble Space Telescope, obtained at the Space Telescope Science Institute, which is operated by the Association of Universities for Research in Astronomy, Inc., under NASA contract NAS5-26555. These observations are associated with program GO-16196, and archival data from programs 11505, 11524, and 17105.



Original content from this work may be used under the terms of the [Creative Commons Attribution 4.0 licence](https://creativecommons.org/licenses/by/4.0/). Any further distribution of this work must maintain attribution to the author(s) and the title of the work, journal citation and DOI.

Abstract

We observed the Seyfert 1 galaxy Mrk 817 during an intensive multiwavelength reverberation mapping campaign for 16 months. Here, we examine the behavior of narrow UV absorption lines seen in the Hubble Space Telescope/Cosmic Origins Spectrograph spectra, both during the campaign and in other epochs extending over 14 yr. We conclude that, while the narrow absorption outflow system (at -3750 km s^{-1} with $\text{FWHM} = 177 \text{ km s}^{-1}$) responds to the variations of the UV continuum as modified by the X-ray obscurer, its total column density ($\log N_{\text{H}} = 19.5^{+0.61}_{-0.13} \text{ cm}^{-2}$) did not change across all epochs. The adjusted ionization parameter (scaled with respect to the variations in the hydrogen-ionizing continuum flux) is $\log U_{\text{H}} = -1.0^{+0.1}_{-0.3}$. The outflow is located at a distance smaller than 38 pc from the central source, which implies a hydrogen density of $n_{\text{H}} > 3000 \text{ cm}^{-3}$. The absorption outflow system only covers the continuum emission source and not the broad emission line region, which suggests that its transverse size is small ($< 10^{16} \text{ cm}$), with potential cloud geometries ranging from spherical to elongated along the line of sight.

Unified Astronomy Thesaurus concepts: Active galaxies (17); Active galactic nuclei (16); Seyfert galaxies (1447)

1. Introduction

Active galactic nuclei (AGNs) stand out as important tools for understanding the evolution of galaxies. In particular, AGN feedback uses the deposition of energy and momentum into the host's interstellar medium (ISM) to help regulate the star formation (e.g., Elvis 2006). One possible contributor to the feedback process is outflows detected as absorption features in AGN spectra (e.g., Silk & Rees 1998; Scannapieco & Oh 2004; Yuan et al. 2018; Vayner et al. 2021; He et al. 2022). These outflows provide a valuable understanding of the dynamics and physical processes occurring within the vicinity of SMBHs at the centers of galaxies.

Absorption lines observed in the rest-frame UV spectra of AGNs are commonly classified into three categories: broad absorption lines (BALs), characterized by a width of $\geq 2000 \text{ km s}^{-1}$; narrow absorption lines (NALs), with a width of $\leq 500 \text{ km s}^{-1}$; and an intermediate group referred to as mini-BALs (Itoh et al. 2020).

Because of the difficulty in distinguishing between intrinsic NALs associated with the quasars and NALs that are unrelated to the quasars (intervening NALs), our understanding of the nature of NAL outflows is limited. Intervening NALs can have diverse origins, including intervening galaxies, intergalactic clouds, Milky Way gas, or gas within the host galaxies of the quasars (Misawa et al. 2007a). Various studies, such as Misawa et al. (2007a), Zhi-Fu Chen (2013), and Chen et al. (2018a), emphasize that observing the variability in the absorption lines is a reliable method to differentiate between NALs originating from an associated outflow and those classified as intervening NALs. These variations in the absorption lines typically result from changes in the ionizing flux striking the absorbing gas.

While NAL outflows have garnered less attention compared to BALs, they may be a valuable tool for probing the physical properties of outflows (for example, Dehghanian et al. 2019 used NALs to explain the physics behind the line–continuum decorrelation observed in the Seyfert galaxy NGC 5548). This potential arises from two key reasons, as outlined by Misawa et al. (2007b):

1. NALs do not suffer from self-blending, a problem created by the merging of blue and red components of doublets like C IV $\lambda\lambda$ 1548, 1551 Å. This simplifies the analysis of NALs, making them advantageous for certain investigations.
2. NALs are found in the spectra of both radio-loud and radio-quiet AGN, whereas BALs are predominantly detected in radio-quiet quasars.

Approximately 50% of Seyfert galaxies and low-redshift AGNs exhibit intrinsic NALs (Crenshaw et al. 1999, 2003; Dunn et al. 2008). Relative to the emission lines, these NALs are blueshifted, commonly with outflow velocities around a few hundred kilometers per second. However, higher-velocity components exceeding 1000 km s^{-1} are also observed in a few objects. Studies employing either variability (e.g., Gabel et al. 2005; Arav et al. 2012; Kriss et al. 2019; Arav et al. 2020) or density-sensitive lines (e.g., Gabel et al. 2005; Arav et al. 2015) locate the narrow absorption outflow gas in proximity to either the obscuring torus or the narrow-line region. These outflow systems could originate from the obscuring torus (Krolik & Kriss 1995, 2001) or potentially from interstellar clouds in close proximity to the nucleus (Crenshaw & Kraemer 2005).

The lower-velocity lines exhibit physical characteristics typical of gas found in the narrow-line region or gas ablated from the torus, and their kinematics align with either a thermal wind originating from the torus or near-nuclear interstellar motions. For the case of the high-velocity lines that reach several thousand kilometers per second, an alternative acceleration mechanism is required. Revalski et al. (2021) observed velocity ranges between 1000 and 2000 km s^{-1} in their study of nearby Seyferts' extended narrow-line regions, for which they suggest in situ radiative acceleration of existing clouds. Another possible scenario is that gas is shocked and entrained by higher-velocity outflows from the AGN itself, as proposed in entrained ultra fast outflow (UFO) models (Gaspari & Sądowski 2017; Sanfrutos et al. 2018; Longinotti et al. 2019; Serafinelli et al. 2019; Mehdipour et al. 2022).

1.1. Seyfert Galaxy Mrk 817: The STORM2 Campaign

The AGN Space Telescope and Optical Reverberation Mapping 2 (STORM2)⁴⁴ project is an intensive spectroscopic reverberation mapping (RM) campaign that observed the Seyfert 1 galaxy Mrk 817 from 2020 to 2022 using the Cosmic Origins Spectrograph (COS; Green et al. 2012), on the Hubble Space Telescope (HST; Peterson et al. 2020). While the primary goal of the project was to determine the kinematics and geometry of the central regions using RM methods (Kara et al. 2021; Cackett et al. 2023; Homayouni et al. 2023, 2024; Partington et al. 2023; Neustadt et al. 2024), the observations revealed additional exciting results: there were significant variations in the response time of the broad UV emission lines to the continuum variations, and there was significant, variable

⁴⁴ The first STORM campaign targeted NGC 5548 (De Rosa et al. 2015).

Table 1
HST/COS Observations

Visit ID	THJD	Date	F1180	Data Source	Grating
09-1	5047.1	2009-08-04	8.22×10^{-14}	COS-GTO (PID ^a : 11505)	G130+G160
09-2	5193.4	2009-12-28	5.91×10^{-14}	COS-GTO (PID:11524)	G130+G160
3n	9202.3	2020-12-18	1.20×10^{-13}	STORM2 (PID:16196)	G130(1096 ^b)+G160
75	9322.4	2021-04-18	1.09×10^{-13}	STORM2 (PID:16196)	G130(1096)+G160
2n	9581.5	2022-01-02	7.95×10^{-14}	STORM2 (PID:16196)	G130(1096)+G160
4d	9634.3	2022-02-24	9.50×10^{-14}	STORM2 (PID:16196)	G130(1096)+G160
A5	10129.8	2023-07-04	1.41×10^{-13}	Kriss et al. (2022; PID:17105)	G130(1096)+G130(1222)+G160

Notes. Details of the “before STORM2” observations (first two rows), the “STORM2” observations (four middle rows), and the “after STORM2” observations (last row). The observation times use “truncated Heliocentric Julian Dates,” defined as THJD = HJD − 2450000. F1180 is the continuum flux at $\lambda 1180 \text{ \AA}$ in $\text{erg cm}^{-2} \text{ s}^{-1} \text{ \AA}^{-1}$.

^a Proposal identification number.

^b Central wavelength in \AA .

absorption in the UV and soft X-rays. Specifically, broad emission lines such as C IV exhibited time lags ranging from 2 to 13 days during different time intervals. These variations are associated with variations in the characteristics of a UV and X-ray obscurer located between the broad-line region (BLR) and the central source (Homayouni et al. 2023).

The significant difference observed in the response time of emission lines is a result of the variations in the properties of an X-ray obscurer (e.g., Kaastra et al. 2014), which appears to be located between the BLR and the central source (Homayouni et al. 2024). The spectral energy distribution (SED) generated by the AGN must traverse the obscurer before reaching the BLR. Kara et al. (2021; hereafter Paper I), show what the “obscured” SED looks like for a single visit; however, owing to the changing obscurer properties (location, column density, covering fraction, etc.), the obscured SED varies for each visit. Partington et al. (2023) studied these obscurers using X-ray spectra from the Neutron Star Interior Composition Explorer (NICER) on board the International Space Station.

Paper I modeled the high-velocity ($v_{\text{outflow}} \approx 3720 \text{ km s}^{-1}$) NAL in Mrk 817 for a single visit on 2020 December (called visit 3n), using both obscured and unobscured SEDs. They identified a set of NALs (including H I, C IV, N V, O VI, Si IV, and S VI) and used them to determine the photoionization structure of the absorption outflow system. Their results indicate that the absorbing gas is ionized by the obscured SED and has a hydrogen column density of $N_{\text{H}} = 10^{19.5} \text{ cm}^{-2}$, and an ionization parameter of $\log \xi = 1 \text{ erg cm s}^{-1}$, corresponding to $\log U_{\text{H}} = -0.25$ as explained below.⁴⁵

In this study, we model the high-velocity NALs observed in seven HST spectra, as listed in Table 1. This includes the observation already modeled in Paper I (visit 3n). Two of the observations date back to 2009; one was conducted in 2023, while the remaining four are from STORM2 observations conducted between 2020 and 2022. We selected these particular STORM2 observations from a pool of 165 available spectra because they are the only ones with such extended wavelength coverage, reaching down to 940 \AA , and so, include the O VI and S VI doublets and higher-order Lyman lines. This broad coverage enhances our ability to construct a well-constrained photoionization model.

We will examine how this high-velocity absorption component fits into the general population of NALs in Seyferts. The STORM2 observations show that this absorption component became noticeable when the obscuring outflow appeared in Mrk 817. This mirrors the behavior of Component 1 in NGC 5548 (Arav et al. 2015; Dehghanian et al. 2019), which was characterized by a high velocity (1350 km s^{-1}) and increased strength when an obscuring outflow appeared in NGC 5548. Both absorption systems are also seen in a variety of ionic species beyond C IV and Ly α .

We investigate whether, in all cases, the NALs responded to the obscured SED. We then employ photoionization models to deduce the total hydrogen column density and the ionization parameters of the outflow system for each visit. This approach enables us to explore the potential variations of the absorption outflow system over almost 14 yr. Our findings reveal that, while the absorption outflow system reacts to both AGN and obscurer variations, it remains notably stable over time.

The structure of the paper is outlined as follows: In Section 2, we describe the observations and data acquisition of Mrk 817. In Section 3, we describe the analysis and explain the methods used in the paper. Section 3 also details the methodologies used to calculate the ionic column densities of the NALs. In Section 4, we describe our photoionization models and report the results for each visit. Finally, Section 5 summarizes the paper and discusses the results.

Here, we adopt a cosmology with $h = 0.696$, $\Omega_m = 0.286$, and $\Omega_\Lambda = 0.714$ (Bennett et al. 2014).

2. Observations

Mrk 817 (PG 1434+590) is a Seyfert 1 galaxy with a systemic redshift of $z = 0.031455$ (Strauss & Huchra 1988) and located at J2000 R.A. = 14:36:22.08 and decl. = +58:47:39.39 (based on the NASA Extragalactic Database, NED).⁴⁶ Falco et al. (1999) later updated the above-mentioned redshift to be $z = 0.031158$, meaning $\Delta cz = 89 \text{ km s}^{-1}$, which translates to <3% decrease in our estimated outflow velocity.

The first series of AGN STORM2 observations targeted Mrk 817 for 165 epochs of HST visits. During these observations, which happened between 2020 November and 2022 February, we used the COS instrument with G130M and G160M gratings to cover the 1070–1750 \AA range in single-orbit visits with an approximately 2 day cadence. Extensive

⁴⁵ The dimensionful ionization parameter ξ is defined as $\xi = \frac{L}{n_{\text{H}} R^2}$ (Tarter et al. 1969; Kallman & Bautista 2001), where L is the ionizing luminosity, and R is the distance from the source. The dimensionless ionization parameter U_{H} is defined in Equation (5).

⁴⁶ NED: <https://ned.ipac.caltech.edu/>. NED is funded by NASA and operated by the California Institute of Technology.

details of the observations can be found in Homayouni et al. (2023). Table 1 summarizes the HST visits discussed in this paper. The visit labeled as “visit 3n” is the same spectrum that is modeled in Paper I. Visits 09-1 and 09-2 are from proposals GO-11505 and GO-11524 performed by Green (2009) and Noll (2009), respectively, and published by Winter et al. (2011). These are “before STORM2” observations. Visits 3n, 75, 2n, and 4d are STORM2 observations (Peterson et al. 2020), and finally, visit A5 is an observation conducted by Kriss et al. (2022) “after STORM2” (program GO-17105). We add that (Penton et al. 2000) discussed the local Ly α forest in Mrk 817 using HST/GHRS data. Mrk 817 was also one of the early targets observed by the COS-GTO team, including the data listed in this paper as visits 09-1 and 09-2.

3. Analysis

After obtaining the data from the Mikulski Archive for Space Telescopes, we identified an absorption outflow system at a velocity of $v_{\text{centroid}} = -3750 \text{ km s}^{-1}$ and with an FWHM of 177 km s^{-1} (measured based on the C IV NAL in visit 3n), with blueshifted ionic absorption lines denoted by red vertical lines in Figure 1. Among the identified absorption lines, several well-known resonance doublets, such as C IV and N V, are observed. Figure 1 shows an example of such an identification. The spectrum shown in this figure belongs to visit 2n (2022 January).

3.1. Ionic Column Densities

As an essential step for comprehending the physical characteristics of the outflow system, we need to determine the ionic column densities (N_{ion}) of the NALs. The most straightforward method for measuring column densities is called the apparent optical depth (AOD) method, in which we assume a uniformly covered homogeneous source (Savage & Sembach 1991). In this method, the first assumption is that

$$I(\lambda) = I_0(\lambda)e^{-\tau(\lambda)}, \quad (1)$$

where $I(\lambda)$ is the intensity, $I_0(\lambda)$ is the modeled intensity without absorption, and $\tau(\lambda)$ is the optical depth as a function of wavelength. The second assumption is the constant opacity of the absorbing material, so when expressing the optical depth as a function of outflow velocity, it is related to the column density per unit velocity $N(v) \text{ cm}^{-2} (\text{km s}^{-1})^{-1}$ (see Equation (8) of Savage & Sembach 1991) by

$$\tau(v) = \frac{\pi e^2}{m_e c} f \lambda N(v), \quad (2)$$

where m_e is the electron mass, e is the elementary charge, f is the oscillator strength, and λ is the wavelength of the transition line, respectively. Because of possible saturation (see below), the AOD method is employed to determine lower limits on N_{ion} for singlets, as well as upper limits for doublets when there are no observable absorption troughs.

In cases where multiple lines of the same ion and energy state are present, the partial covering (PC) method can be utilized. This assumes a homogeneous source that is partially covered by the outflow (Barlow et al. 1997; Arav et al. 1999a, 1999b). When using the PC method, phenomena such as nonblack saturation are taken into account since a velocity-dependent covering factor is deduced (de Kool et al. 2002). For

doublets with f value ratio of 1:2, the covering fraction $C(v)$ and the optical depth $\tau(v)$ can both be calculated (Arav et al. 2005) as

$$I_R(v) - [1 - C(v)] = C(v)e^{-\tau(v)} \quad (3)$$

and

$$I_B(v) - [1 - C(v)] = C(v)e^{-2\tau(v)}, \quad (4)$$

where $I_R(v)$ is the normalized intensity of the red absorption feature, $I_B(v)$ is the normalized intensity of the blue absorption feature, and $\tau(v)$ is the optical depth of the red component. Whenever the PC method is used, the final result is a measurement rather than an upper or lower limit. For the doublets of C IV, O VI, and Si IV, we assume an f value ratio of 1:2, since this approximation is less than 2% different from their actual f values reported by Morton (2003).

A detailed comparison between the PC prediction and numerical calculations of the optical depth of a clumpy medium showed the PC method to be surprisingly accurate even when the clumps evolve in a turbulent flow (Waters et al. 2017). For a more detailed explanation of different methods used to calculate ionic column densities and for a deeper understanding of the underlying logic and mathematical aspects, please see Barlow et al. (1997), Arav et al. (1999a, 1999b), de Kool et al. (2002), Arav et al. (2005), Borguet et al. (2012a), Byun et al. (2022b, 2022c), and Dehghanian et al. (2024). In the following three subsections, we separately explain how we dealt with the various spectra and what lines were identified in each.

3.1.1. STORM2: Visits 3n, 75, 2n, and 4d

These observations are part of the STORM2 project and were obtained between 2020 and 2022. For each individual spectrum, we identified the resonance doublets of the C IV, Si IV, N V, O VI, and S VI absorption lines, along with the Ly α , Ly γ , and C III absorption lines. Figure 1 shows the spectrum and absorption lines for visit 2n. The other three spectra are very similar to the spectrum shown in Figure 1.

It is essential to highlight that, as explored in Paper I by modeling the N V and O VI doublets, the narrow absorption outflow system primarily covers the continuum source emission rather than the BLR emission. Figure 2 confirms the same situation is happening for Ly α . A detailed examination of the C IV NAL also supports the conclusion that its narrow absorption covers only the continuum and not the BLR. Based on these findings, it is appropriate to consider only the partial coverage of the continuum source and exclude any coverage of the BLR throughout this paper. This situation also occurs in some BAL outflows (e.g., Figure 1(c) in Arav et al. 1999b). In Section 5, we further discuss this by establishing an upper limit for the location of the outflow.

Figure 2 illustrates how we incorporate this assumption into our calculations. We use a power law for the continuum and then fit the emission lines with Gaussian[s] to model the data. To produce Figure 2, we subtract the continuum level from the emission model, resulting in an “emission-only” model (depicted by the orange curve in Figure 2). Because the depth of the absorption line is equal to the subtracted continuum, we know that the absorber is only affecting the continuum and not the BLR emission. The same is true for the N V and O VI NALs (see Paper I). Combined, these independent observations strongly suggest that the outflow only covers the continuum

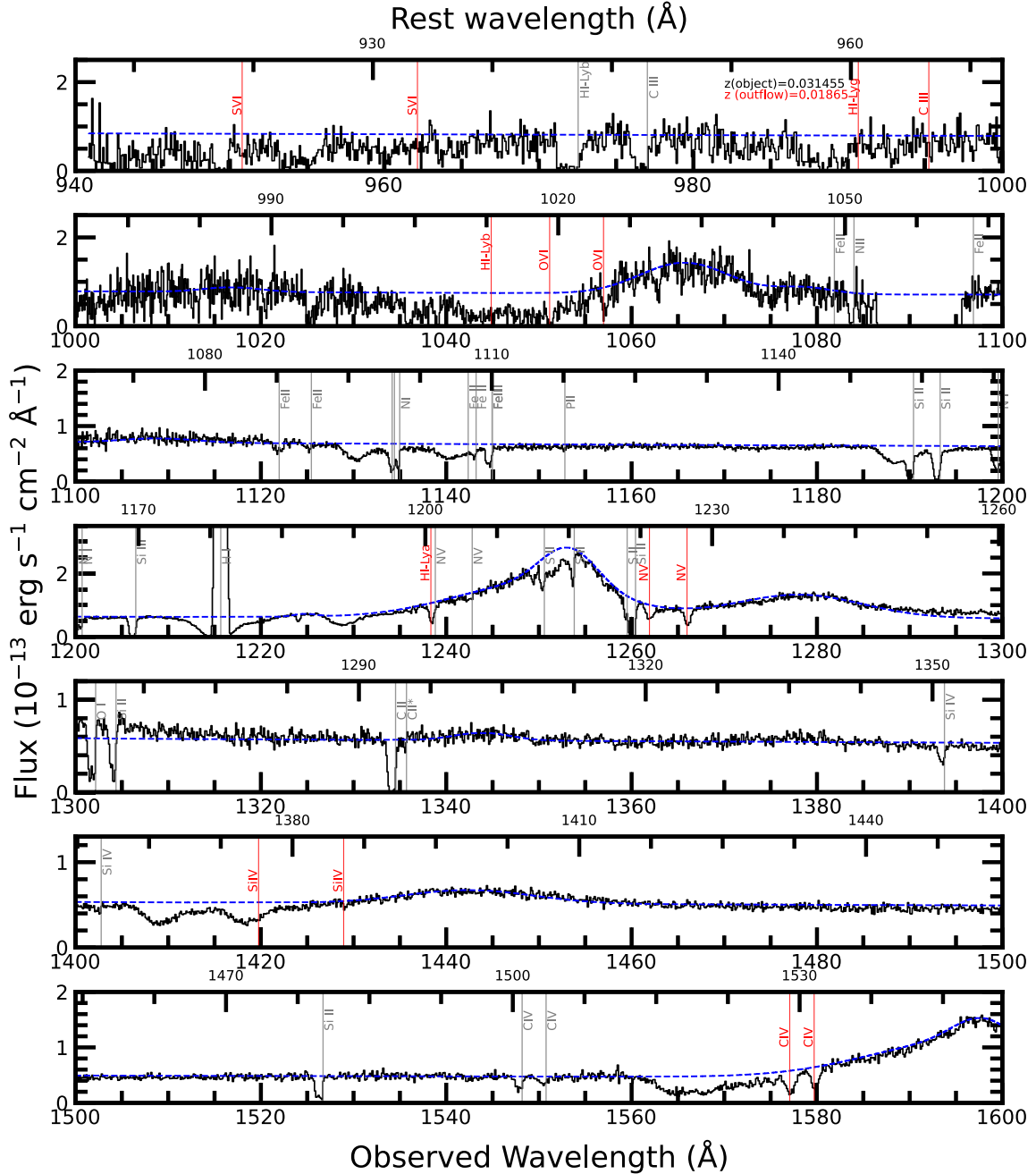


Figure 1. The 2022 January HST/COS spectrum of Mrk 817 (visit 2n). Red lines indicate the absorption features of the outflow system at a velocity of -3750 km s^{-1} . Absorption from the Galactic interstellar medium (ISM) is shown with vertical gray lines. The Galactic absorption along this sight line includes strong blueshifted components (Collins et al. 2003; Fox et al. 2023). The dashed blue line shows our continuum plus broad-line emission model. The spectrum also shows broader higher-velocity outflow systems such as the C IV trough between 1560 and 1570 Å observed wavelength. Details for that system are given in Paper I.

source. Subsequently, we subtract this “emission-only” model (orange curve) from the total flux and model the NALs under the assumption that they only cover the continuum emission and do not cover the BLR.

For each NAL, we transferred the emission-subtracted normalized flux from wavelength space to velocity space in the rest frame of Mrk 817 at $z = 0.031455$, using z_{outflow} . Figure 3 shows this concept for visit 2n. To calculate the ionic column densities, we have chosen an integration range of -3900 to -3600 km s^{-1} (shown with vertical orange lines). This region was selected based on the centroid velocity and the width of the absorption trough of C IV. As all the absorption

lines originate from the same outflow system, we employ the same integration range for all of them.

To calculate the ionic column density of the C IV doublet, we employ the PC method and consider the results as a measurement. Since Si IV is shallow and weak, we use the AOD method and consider the results an upper limit. While H I-Lyα is actually a doublet due to its upper state having fine structure, it is treated as a singlet. The reason is that the energy levels of the fine structure are extremely close, so they cannot be separated spectroscopically. For this reason, the column density of Lyα is taken to be a lower limit, which is also consistent with saturation at full coverage of only the

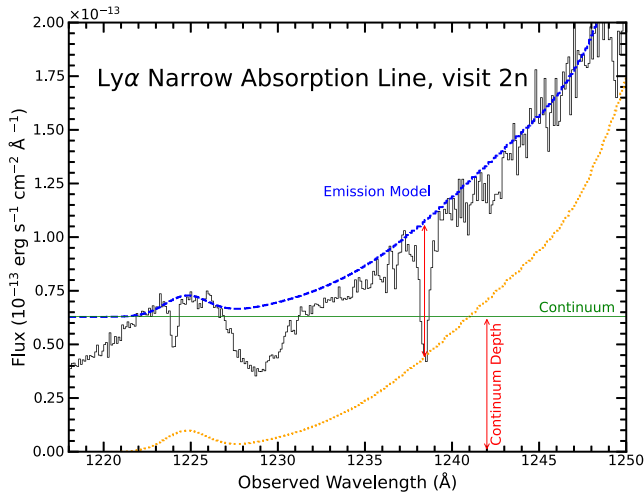


Figure 2. The visit 2n HST/COS spectrum of the Ly α surrounding region (black). The best-fit emission plus the continuum model is in blue; the model continuum is anchored in the line-free region at around 1200 Å and is shown in green. The orange line shows the continuum-subtracted emission model. Both of the red arrows have the same length, which is equal to the depth of the continuum. It is clear that the depth of the absorption trough is exactly equal to the continuum depth, indicating that it fully (and only, see Section 3.1.1) covers the continuum emission.

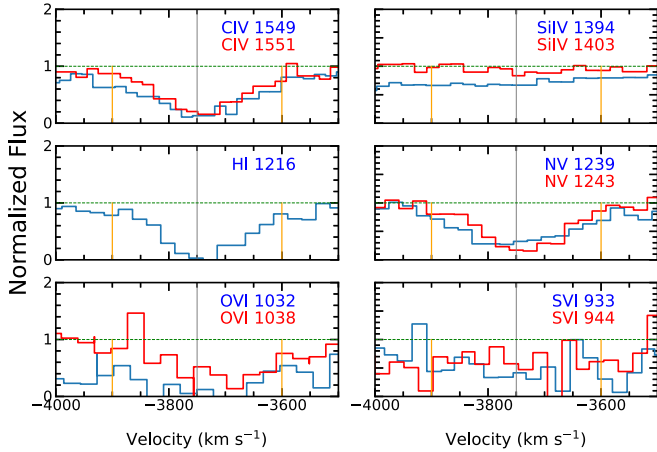


Figure 3. Normalized flux (after subtracting the emission lines, see Figure 2) vs. velocity for blueshifted absorption lines detected in the spectrum of Mrk 817 in 2022 January (visit 2n). The continuum level is shown by the horizontal green dashed line. The integration range (-3900 to -3600 km s $^{-1}$) is shown with vertical orange lines, while the centroid velocity of $v_{\text{centroid}} = -3750$ km s $^{-1}$ is shown with a solid black line.

continuum (see Figure 2), based on the AOD method. It is also blended with the ISM N V 1238 Å absorption line (as shown in the fourth panel of Figure 1). However, higher-order lines of the Lyman series are also covered in all STORM2 spectra, so we use Ly γ as an upper limit for H I column density. We do not use Ly β since, as Figure 1 shows, it is contaminated by the O VI broad absorption trough. The ionic column densities of N V, O VI, and S VI were determined using the AOD method and are considered to be lower limits due to being saturated. C III's ionic column density is also measured using the AOD method and is considered a lower limit. While we only show the velocity plot for visit 2n, the same behavior was observed in visits 3n, 4d, and 75; hence, the same consideration will be applied to all visits. Table 2 provides the values of measured column density for each ion. The adopted uncertainties include

Table 2
The Ionic Column Densities, STORM2

Ion	Visit 3n	Visit 75	Visit 2n	Visit 4d
C IV	440^{+60}_{-55}	340^{+78}_{-69}	774^{+220}_{-108}	709^{+140}_{-90}
Si IV	$<21^{+3}$	$<12^{+3}$	$<14^{+3}$	$<7^{+2}$
H I-Ly α	$>93_{-10}$	$>90_{-11}$	$>270_{-75}$	$>100_{-18}$
H I-Ly γ	$<900^{+400}$	$<1140^{+600}$	$<1200^{+500}$	$<1500^{+600}$
N V	$>726_{-85}$	$>490_{-45}$	$>900_{-101}$	$>850_{-104}$
S VI	$>113_{-45}$	$>112_{-47}$	$>116_{-84}$	$>134_{-53}$
O VI	$>1808_{-340}$	$>1500_{-480}$	$>1080_{-428}$	$>1900_{-455}$
C III	$>45_{-7}$	$>50_{-20}$	$>54_{-27}$	$>59_{-25}$

Note. The column densities are in units of 10^{12} cm $^{-2}$. We determine the lower limits using AOD measurements based on a Gaussian fit to the spectrum, accounting for blending and saturation. For upper limits, where absorptions are too shallow, we treat the AOD results as upper limits, adding a positive uncertainty. This approach ensures that we consider both finite lower [upper] and infinite upper [lower] uncertainties, as well as systematic errors.

the corresponding PC (for C IV) or AOD (for the rest of the lines) uncertainties and a systematic error of 10%, added in quadrature (e.g., Miller et al. 2018; Xu et al. 2018; Miller et al. 2020c; Dehghanian et al. 2024). The measurements reported for visit 3n slightly differ from the ionic column densities previously published in Paper I. These minor differences are due to different measurement techniques, and the results are consistent within the uncertainties.

While we investigate the properties of the outflow system and its possible variations later in Sections 3 and 5, it is worth mentioning that the depth of the absorption (the optical depth) varies from one visit to another, as shown for C IV in Figure 10 of Paper I. Figure 4 compares two examples of such variations (Ly α and C IV absorption lines) by comparing the line profiles in detail.

3.1.2. Before STORM2: Visits 09-1 and 09-2

In 2009, Mrk 817 was observed as a part of two non-STORM2 observing projects (Green 2009; Noll 2009; Winter et al. 2011). In both cases, the observations were obtained using COS with G130M and G160M gratings. These data sets are named visits 09-1 (Noll 2009) and 09-2 (Green 2009) in Table 1, and both showed narrow Ly α absorption lines in their spectrum. In both cases, since the Ly α absorption is not saturated and is much shallower than the troughs observed in the STORM2 visits, we consider it as a measurement. For both of these visits, we could barely identify C IV and N V absorption doublets. Given that these doublets are very shallow and are comparable to the level of the noise, we treat them as upper limits. These measurements are presented in Table 3 and will be subsequently employed in the photoionization modeling.

3.1.3. After STORM2: Visit A5

The most recent spectrum of Mrk 817 that we discuss here was obtained from HST observations of the source in 2023 July (Kriss et al. 2022). We identified the same absorption system in this spectrum through the Ly α , O VI, and N V NALs. Since the weak Ly α line is similar to the 2009 visits, we again take the estimates from the Ly α as a measurement, while the column density of the O VI doublet is measured via the AOD method and taken as a lower limit due to being saturated. We also

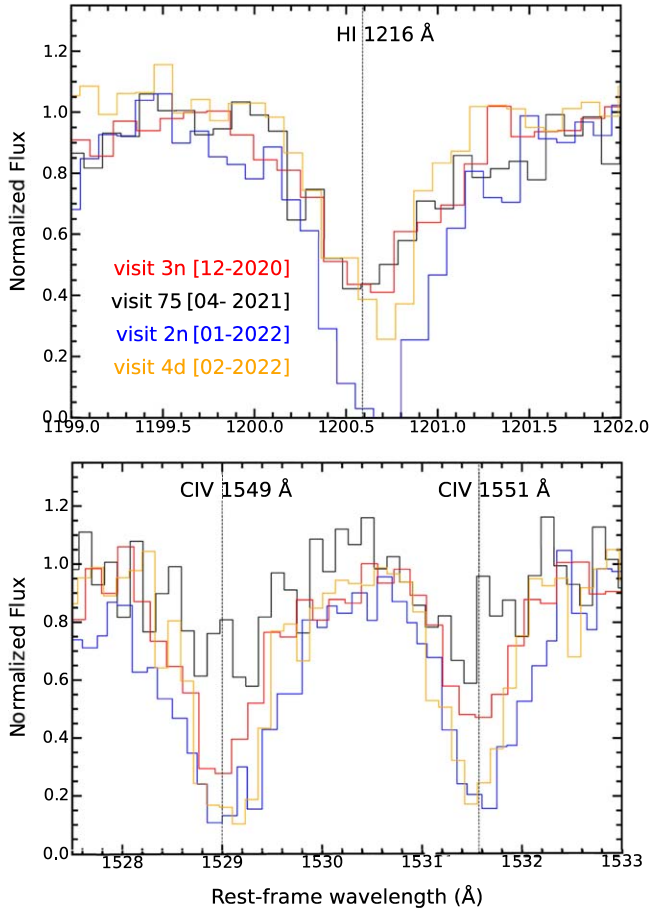


Figure 4. Top panel: the normalized flux in $\text{Ly}\alpha$ absorption wavelength region from four STORM2 spectra. Bottom panel: the normalized flux in the C IV absorption wavelength region. The vertical dashed lines indicate the centroid wavelength of the absorption trough based on z_{outflow} . Both panels show the normalized data after subtracting the emission model (see Figure 2).

Table 3
The Ionic Column Densities, Non-STORM

Ion	Visit 09-1	Visit 09-2	Visit A5
H I- $\text{Ly}\alpha$	38^{+5}_{-4}	42^{+9}_{-9}	40^{+10}_{-11}
Si IV	$<5^{+3}$	$<7^{+3}$	$<13^{+7}$
C IV	$<25^{+5}$	$<27^{+4}$	$<35^{+7}$
O VI	$>460_{-190}$
S VI	$<63^{+23}$
N V	$<38^{+6}$	$<45^{+6}$	73^{+8}_{-5}

Note. The column densities are in units of 10^{12} cm^{-2} .

identified the NV doublet, and since it did not seem to be saturated, we took it as a measurement, too. We have also identified shallow troughs of C IV, Si IV, and S VI that can serve as upper limits. Table 3 reports the adopted value for each of the mentioned ionic column densities.

Figure 5 compares the $\text{Ly}\alpha$ absorption troughs in one of the STORM2 visits (visit 3n) with one of the 2009 visits (visit 09-1) and the 2023 visit (visit A5). As illustrated in this figure, the $\text{Ly}\alpha$ observations from 2009 and 2023 exhibit similar depth, and both are shallower than the $\text{Ly}\alpha$ absorption observed in 2020 December (visit 3n). This pattern supports the idea that AGN

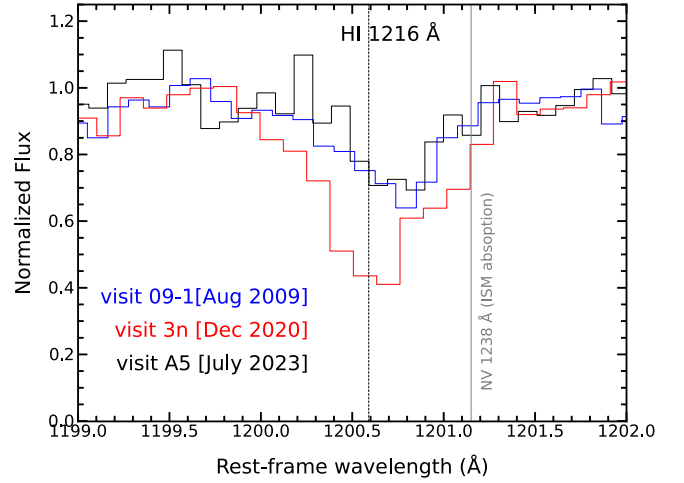


Figure 5. The $\text{Ly}\alpha$ narrow absorption lines within visit 3n (STORM2) and visits 09-1 and A5 (both non-STORM2). The vertical dashed line indicates the centroid wavelength of the absorption trough based on z_{outflow} .

was in a higher ionization state in 2009 and 2023 compared to 2020.

4. Photoionization Solutions

The primary aim of this study is to estimate the properties of the absorption outflow system, including its total hydrogen column density (N_{H}) and its ionization parameter (U_{H}), and measuring the ionic column densities was the first step toward that goal (e.g., Byun et al. 2022a, 2022b, 2022c; Dehghanian et al. 2024). The next step is to produce a grid of N_{H} and U_{H} using Cloudy simulations (Chatzikos et al. 2023). These simulations predict the ionic column density of each ion for each combination of N_{H} and U_{H} . Cross-matching these predictions with the values deduced in Section 3 leads us to the outflow’s N_{H} and U_{H} .

We start this process by producing the appropriate SED for each visit. Because of the presence of the obscurer, for each visit, we have two SEDs, an “unobscured SED” (i.e., the intrinsic continuum) that irradiates the obscurer, as well as the “obscured SED” that illuminates the farther-away surrounding gas. As discussed (and shown) in Paper I, the NALs outflow system is ionized by the obscured SED, implying that the obscurer is located between the outflow system and the source.

For each visit, we obtain the “unobscured” and the “obscured SED” by combining the results of Paper I and Partington et al. (2023) as follows: In Paper I, the global model for the broadband continuum of Mrk 817 was established for one epoch (Visit 3n) using extensive HST and XMM-Newton observations. We adopt the “warm Comptonization” version of this model in light of the multiwavelength variability characteristics of Mrk 817. In Partington et al. (2023), the parameters of the X-ray continuum and the obscurer (column density, covering fraction, and ionization parameter) are derived for other epochs using NICER monitoring observations. Therefore, by tracing changes in the continuum and the obscurer parameters compared to the visit 3n, the unobscured and obscured SEDs for the other visits were calculated. For each visit, the far-UV part of the broadband continuum from Paper I is matched to the observed HST spectrum by fitting the temperature of the disk blackbody component of the SED. In the case of the 2009 HST visits, which have no joint X-ray

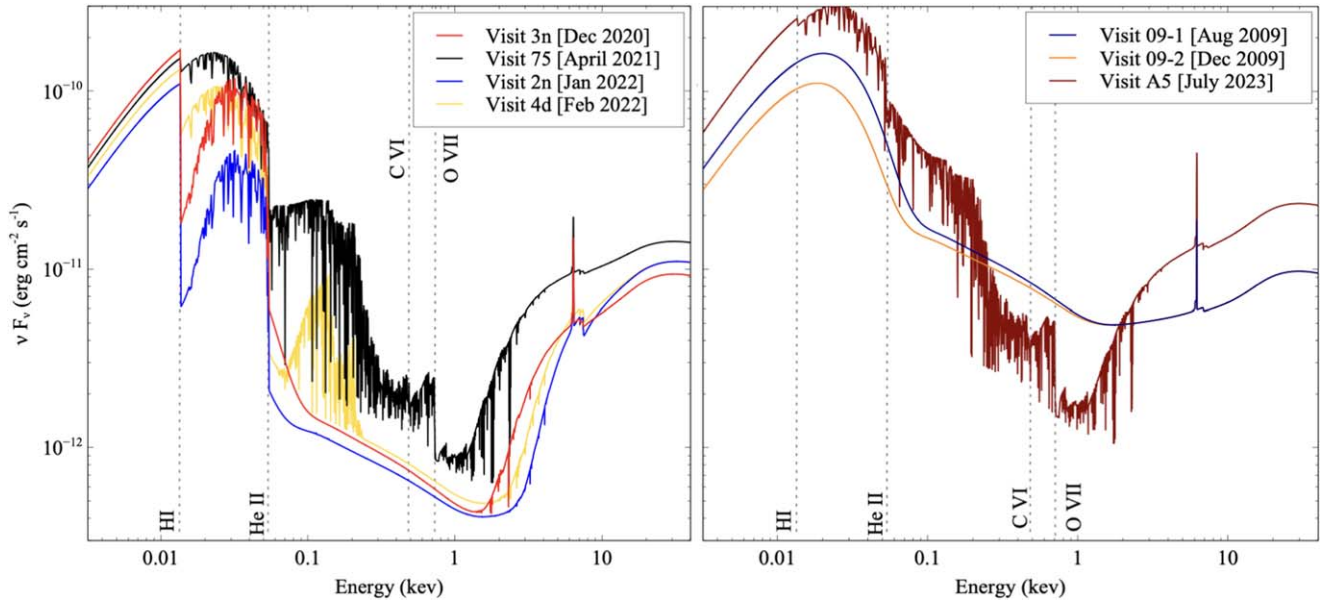


Figure 6. The SEDs used in the photoionization models (see Section 4 for details). Left panel: the SED illuminating the narrow absorption outflow system during the STORM2 visits. Right panel: the SED illuminating the narrow absorption outflow system during non-STORM2 visits. In both panels, the opacity sources of H I (at 13.6 eV), He II (at 54.4 eV), and the K-shell edges of carbon (C VI at 489.99 eV), and oxygen (O VII at 739.32 eV) are shown as dashed vertical lines.

observations, the X-ray part of the unobscured SED from visit 3n is adopted. Figure 6 illustrates the SEDs used for each single visit.

With the required SEDs in hand, we produce Cloudy photoionization model grids to predict the characteristics of the outflow system. We use a fixed gas hydrogen density of $n_{\text{H}} = 10^4 \text{ cm}^{-3}$ after verifying that the results are not dependent on the density for $n_{\text{H}} < 10^{11} \text{ cm}^{-3}$. Figure 7 displays the results of such calculations for STORM2 visits. Additionally, Figure 8 presents the same results for the case of visit A5.

In each panel of Figures 7–9, the colored contours match the values reported in Tables 2 and 3. We exclude visit 09-2 because the only measurement available for this visit is Ly α while the upper limits implied by C IV, N V, and Si IV are trivially satisfied. Therefore, the photoionization solution can be anywhere along the H I constraint. For each visit, and by employing χ^2 minimization methods (Arav et al. 2013), we narrowed down the column density–ionization parameter space to a pair of N_{H} and U_{H} for the absorption outflow system. An absorption outflow system characterized by these N_{H} and U_{H} values yields the ionic column densities and their associated uncertainties given in Tables 2 and 3. The results of these simulations are detailed in Table 4. Note that solar abundances were assumed to produce these results. Due to the limited number of absorption lines identified in the two 2009 visits, which include only one measurement (Ly α) and three upper limits (C IV, Si IV, and N V), there is considerable uncertainty associated with their N_{H} and U_{H} .

5. Discussion

Figures 10–12 show how the measured column densities and two versions of the ionization parameter vary during 14 yr. Figure 10 compares the total hydrogen column density of the absorption outflow system in each visit. Additionally, we include the measurements reported by Paper I, consistent with

our results. The value of N_{H} is consistent between all epochs, supporting the assertion that this is the same stable outflow.

Figure 11 shows the ionization state of the absorption outflow system varies over time. We include the value of the ionization parameter measured by Paper I (Kara et al. 2021) ($\log \xi = 1$). Incorporating the best-fit values for the obscured SED in visit 3n, $\log \xi = \log U_{\text{H}} + 1.25$. This implies that Paper I’s ionization parameter converts to $\log U_{\text{H}} = -0.25$, which is shown by the yellow circle in this figure.

While the ionization parameter of the absorption outflow system is accurately measured for each visit, its value is affected by the AGN’s flux variability as well as the variations of the obscurer from one visit to another. To understand this effect and to focus on the outflow’s variations, it is crucial to consider only the integrated ionizing flux rather than only the observed UV flux. From the SED, We measure the $Q(\text{H})$, the number of hydrogen-ionizing photons emitted by the central object per second (Osterbrock & Ferland 2006). It is related to the ionization parameter by

$$U_{\text{H}} \equiv \frac{Q(\text{H})}{4\pi R^2 c n_{\text{H}}}. \quad (5)$$

So for a constant hydrogen density and constant distance from the source,

$$\Rightarrow U_{\text{H}} \propto Q(\text{H}). \quad (6)$$

According to the equation above, we can adjust the ionization parameter using $Q(\text{H})$ for each visit. Figure 12 shows the results. To produce this figure, we first calculated the effects of SED variations on U_{H} (by calculating $Q(\text{H})$) and then scaled all ionization parameters with respect to one visit (visit 2n). This illustrates the variations of the outflow’s ionization parameter, which are independent of the AGN’s flux variability or the presence of the obscurer.

As depicted in Figure 12, the measurements are consistent within the measured uncertainties. Drawing from these results

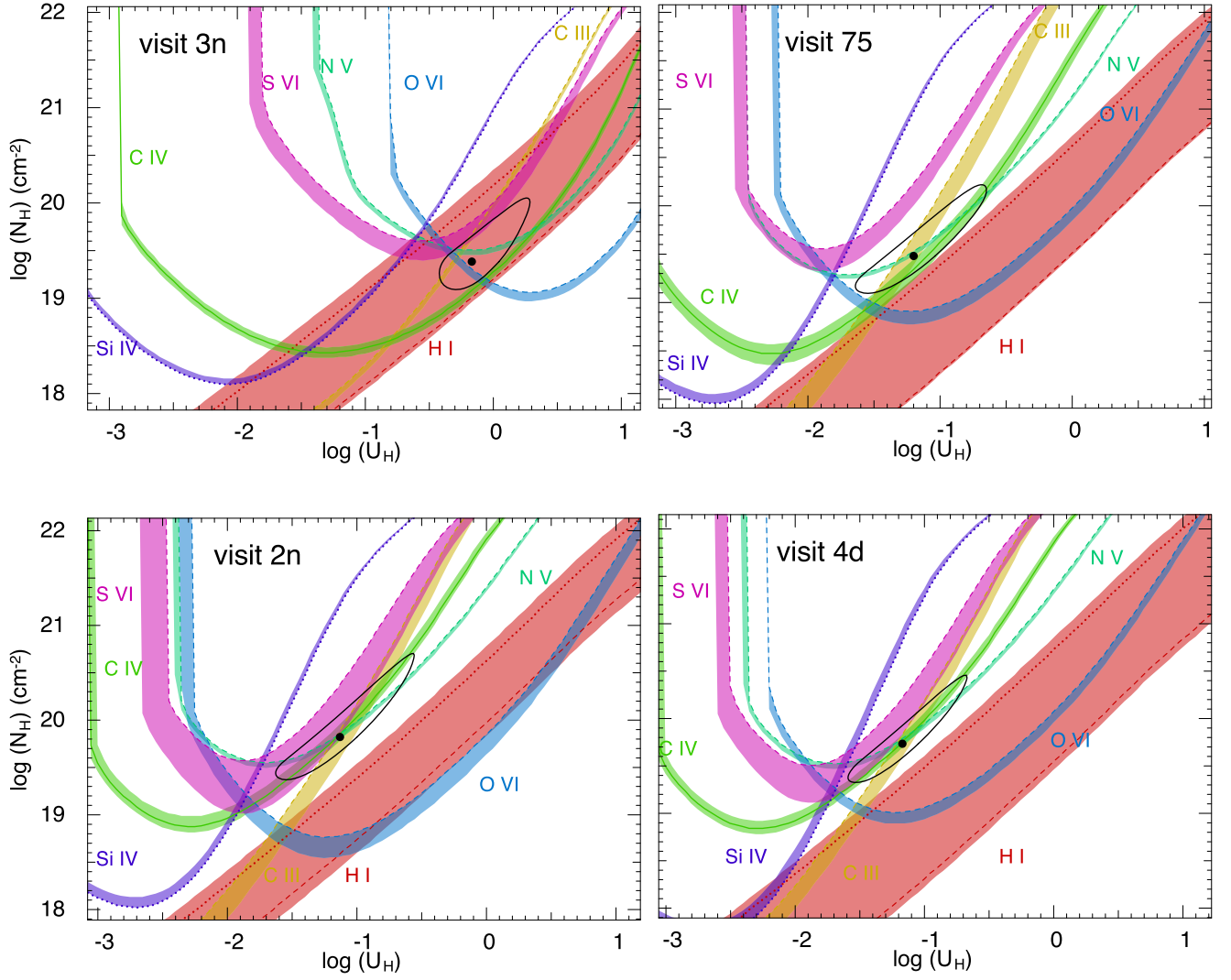


Figure 7. All four panels present single-phase photoionization solutions for the absorption outflow system per STORM2 visits. Each colored contour represents the ionic column densities consistent with the observations (refer to Table 2), assuming the appropriate spectral energy distribution (SED) and solar metallicity. In all four panels, the C IV contour (green) consists of a solid line that indicates an actual measurement, while the upper and lower uncertainties form the contour's width. The dashed lines inside contours indicate that the estimated column density is indeed a lower limit. Dotted lines indicate the upper limits. Shaded bands depict the uncertainties added for each contour. The black circle denotes the best χ^2 -minimization solutions, and the 1σ confidence region is represented by a black contour.

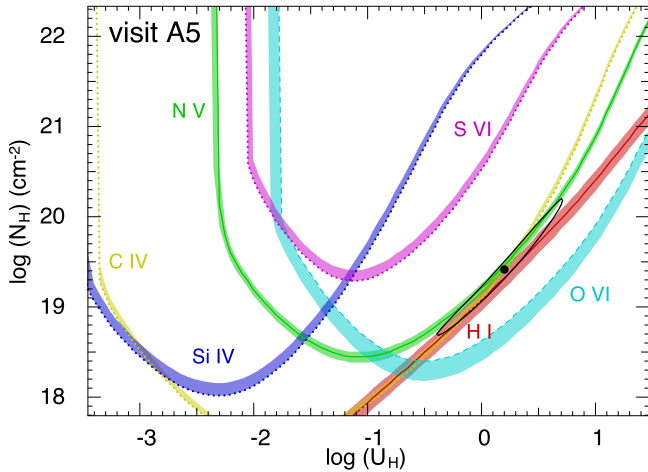


Figure 8. Same as Figure 7, for non-STORM2 visit A5. Here, we adopted the SED labeled as visit A5 in the left panel of Figure 6.

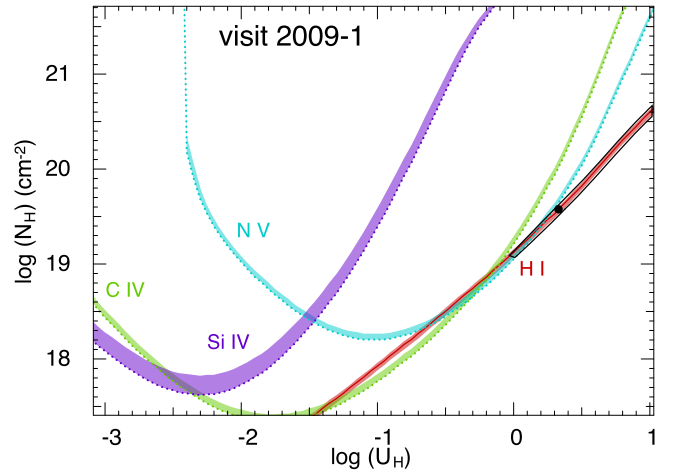


Figure 9. Same as Figure 7, for non-STORM2 visit 2009-01. Here, we adopted the SED labeled as visit 09-1 in the left panel of Figure 6.

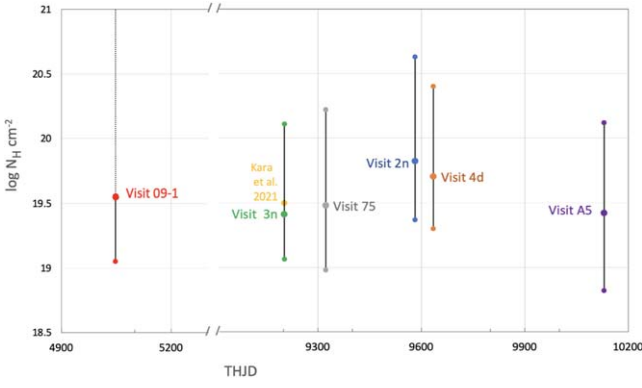


Figure 10. The hydrogen column density determined for each HST visit discussed here. We have also presented the column density measured by Paper I for visit 3n. For each visit, the actual measurement is shown by a larger circle, while smaller circles indicate the upper and lower uncertainties. For visits 09-1 and 2, the dotted portion of the plot points to the large uncertainty in the value of the error.

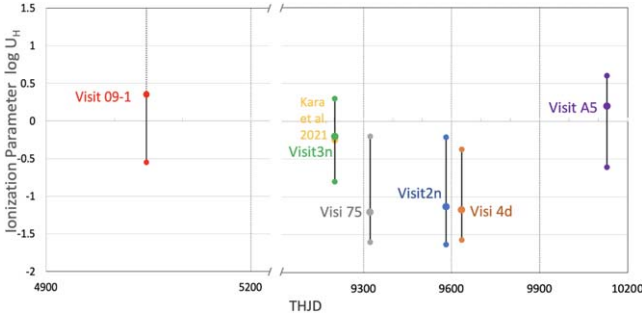


Figure 11. The ionization parameter U_H determined for each HST visit discussed here. We also present the ionization parameter measured by Kara et al. (2021) for visit 3n. For each visit, the actual measurement is shown by a larger circle, while smaller circles indicate the upper and lower uncertainties. For visit 09-1, the dotted portion of the plot points to the large uncertainty in the value of the error.

Table 4
Photoionization Solution

Visit ID	$\log N_H \text{ (cm}^{-2}\text{)}$	$\log U_H$	Adj. $\log U_H$
09-1	$19.55^{+3.00}_{-0.50}$	$0.35^{+1.50}_{-0.91}$	$-0.55^{+1.50}_{-0.91}$
3n	$19.41^{+0.70}_{-0.35}$	$-0.20^{+0.51}_{-0.60}$	$-0.70^{+0.51}_{-0.60}$
75	$19.48^{+1.00}_{-0.51}$	$-1.20^{+0.60}_{-0.42}$	$-1.90^{+1.00}_{-0.42}$
2n	$19.82^{+0.81}_{-0.45}$	$-1.13^{+0.90}_{-0.50}$	$-1.13^{+0.90}_{-0.50}$
4d	$19.70^{+0.71}_{-0.40}$	$-1.17^{+0.81}_{-0.41}$	$-1.67^{+0.81}_{-0.41}$
A5	$19.42^{+0.70}_{-0.60}$	$0.20^{+0.42}_{-0.81}$	$-0.88^{+0.42}_{-0.81}$

Note. Adjusted $\log U_H$ is a version of the ionization parameter that is scaled based on the variations of the SED. More details are available in Section 5.

and the outcomes of the column density calculations, we estimate that the outflow system possesses an adjusted ionization parameter $\log U_H = -1.0^{+0.1}_{-0.3}$ and a total hydrogen column density of $\log N_H = 19.5^{+0.61}_{-0.13} \text{ cm}^{-2}$. To estimate the uncertainties for $\log N_H$, we took into account the lower limit from visit 2n and the upper limit from visit 3n. This guarantees that $\log N_H$ always works for all visits, even in its maximum or minimum limits. The same argument works for $\log U_H$ for

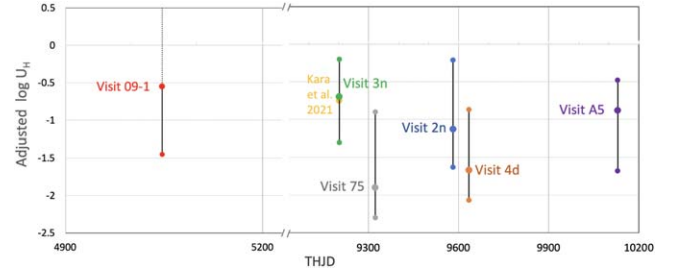


Figure 12. Similar to Figure 11. Here, the ionization parameters are adjusted with respect to the variations of the $Q(H)$ (see text).

which the upper and lower limits are based on visits 3n and 75, respectively.

As demonstrated by both Tables 2 and 3, the ionic column density derived for the $\text{Ly}\alpha$ absorption line exhibited variability over a 14 yr period. This variability suggests that the narrow absorption outflow system is associated with the AGN rather than being an intervening system. This serves as motivation to determine the location of the NAL outflow system. Due to the absence of density-sensitive, excited-state NALs in the examined HST visits, we were unable to pursue the methods presented in Byun et al. (2022b, 2022c) and Dehghanian et al. (2024) for determining the location. However, following the discussion in Arav et al. (2012), we can obtain limits on the electron density based on the limits on the observed recombination time, which then results in an upper limit on the distance for the outflowing gas. We use their discussion to estimate the electron density of the outflow based on the $\text{Ly}\alpha$ variability during a certain period of time:

$$t^* = \left[-f \alpha_i n_e \left(\frac{n_{i+1}}{n_i} - \frac{\alpha_{i-1}}{\alpha_i} \right) \right]^{-1}, \quad (7)$$

in which t^* is the timescale for changes in the ionic fraction, f is a scaling factor or ionic fraction, and α_i is the recombination rate coefficient for the ionization state i . n_e is the electron density, while $\frac{n_{i+1}}{n_i}$ is the ratio of the number densities of the next ionization state ($i+1$) to the current state (i). And finally, $\frac{\alpha_{i-1}}{\alpha_i}$ is the ratio of recombination coefficients between the ionization state ($i-1$) and the current state (i).

We set limits on the recombination time, t , by considering the shortest time span between two visits that exhibit unambiguous changes in $\text{Ly}\alpha$ absorption. Since STORM2 observations show significant $\text{Ly}\alpha$ absorption variations between adjacent epochs separated by 2 days, we determine an upper limit on the recombination time of 2 days. However, it is plausible that the actual recombination time is smaller, so we treat the derived density as a lower limit, resulting in an upper limit for the location, denoted as r_{max} .

To proceed with our calculations, Cloudy 23.0 (Chatzikos et al. 2023) was employed to determine the ratio of $\frac{n_{i+1}}{n_i}$ for a narrow absorption outflow system that is ionized by the SED corresponding to visit 2n. Following the discussion in Krolik & Kriss (1995) and assuming equilibrium, we can take $f = -1$. Consequently, our analysis yields a calculated upper limit for the electron density to be $\log n_e > 3.46 \text{ cm}^{-3}$ or $\log n_H > 3.5 \text{ cm}^{-3}$. We then solve Equation (5) to compute the corresponding location, resulting in a value of $r_{\text{max}} = 38 \text{ pc}$ for the distance between the NAL outflow system and the central source.

As discussed in Paper I and also in Section 3.1.1 here, resolving the peculiar depth ratios of the N V, C IV, and O VI doublet troughs is achievable if the narrow-line absorption only covers the continuum source. Paper I speculated that this suggests the NAL outflow system is located within the interior of the BLR. Alternatively, another possible scenario is that the narrow absorbing cloud is relatively small, sufficiently covering the continuum-emitting region $\sim 100 R_g \approx 5.7 \times 10^{14}$ cm, for a black hole mass of $3.85 \times 10^7 M_\odot$ (Bentz & Katz 2015) but not large enough to encompass a substantial portion of the BLR (~ 10 light days or 2.6×10^{16} cm; Kara et al. 2021; Homayouni et al. 2023). Its low hydrogen density ($> 3000 \text{ cm}^{-3}$) and a column density of $3 \times 10^{19} \text{ cm}^{-2}$ suggest a maximum thickness of 1×10^{16} cm for the cloud. Thus, regarding its small size, it could take on a quite elongated “string” shape with an aspect ratio of $\sim 15:1$. Its high velocity and possible elongated morphology might suggest it is material that has been entrained in a faster outflow, perhaps one of the UFOs identified by Zak et al. (2024). However, if the cloud instead has a density of $3 \times 10^5 \text{ cm}^{-3}$ (typical of the narrow-line region in other Seyferts like NGC 5548, e.g., Arav et al. 2015), which locates it much closer to the source (3.8 pc), it would be consistent with being spherical.

If the cloud is small in diameter, the fact that its properties in absorbing the continuum are stable suggests that its transverse motion must be small. To put this into perspective, considering a cloud with a diameter of 5.7×10^{14} cm, for it to traverse this distance in less than 14 yr, its transverse velocity would need to be approximately 13 km s^{-1} . In contrast, the Keplerian velocity around the black hole in Mrk 817 (with a mass of $3.85 \times 10^7 M_\odot$) ranges between 209 and 66 km s^{-1} for radii spanning from 3.8 to 38 pc. Although the limit of 13 km s^{-1} falls below these estimates, clouds with several times larger diameters could still effectively obscure the continuum without substantially covering the BLR.

The high-velocity NALs in Mrk 817 have become noticeable specifically during the epochs in which the X-ray obscurer exists. This phenomenon is observed in various cases, such as Component 1 in NGC 5548 (Arav et al. 2015) and the stronger Ly α line witnessed in the recent obscuring event in MR2251-178 (Mao et al. 2022). Notably, these lines were present previously but gained prominence only during the obscuration of the ionizing continuum. This suggests that the observed gas normally exists in a fairly high ionization state with only Ly α and other high-ionization lines weakly visible at all. Their presence becomes more prominent when the ionizing continuum is significantly diminished due to obscuration, lowering the ionization state of the gas and making lower ionization species more prominent. These large-scale outflows could originate from a torus (e.g., Dorodnitsyn et al. 2008, 2016), from an outer accretion disk (e.g., Waters et al. 2021), or from inflows (e.g., Proga 2007; Kurosawa & Proga 2009; Mościbrodzka & Proga 2013).

6. Summary

In this paper, we examined the narrow absorption outflow system in seven distinct spectral epochs of Mrk 817, all observed by HST between 2009 and 2023. We identified several NALs in each visit and subsequently measured the ionic column densities, which were later employed for photoionization modeling purposes. The detailed results are presented in Table 4. Our analysis of the absorption outflow

system in Mrk 817, spanning seven separate HST spectra from 2009 to 2023, has provided insights into the system’s stability, i.e., consistent N_H and U_H . We summarize our results as follows:

1. We have identified the same high-velocity NAL outflow system in all seven HST visits spanning over 14 yr.
2. The narrow absorption outflow system is ionized by the “obscured” SED, confirming that the obscurer is between the narrow absorption cloud and the central source.
3. Based on our findings, we estimate that the outflow system has an “adjusted” ionization parameter $\log U_H = -1.0^{+0.1}_{-0.3}$ and a total hydrogen column density of $\log N_H = 19.5^{+0.61}_{-0.13} \text{ cm}^{-2}$. We determine that this outflow system is connected to the AGN and is situated at a distance of < 38 pc from the central source. It also has a hydrogen gas number density whose value exceeds 3000 cm^{-3} .
4. The observed consistency in N_H across all visits and variations in U_H that are in concert with a response to changes in the ionizing continuum suggest that the outflow system has been persistent throughout the a 14 yr period.

























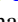
















Acknowledgments

We express our appreciation to the anonymous reviewer whose feedback has contributed to the enhancement of this manuscript. All of the data presented in this paper were obtained from the Mikulski Archive for Space Telescopes (MAST) at the Space Telescope Science Institute. The specific observations analyzed can be accessed via [10.17909/16n2-nt70](https://doi.org/10.17909/16n2-nt70). Our project began with the successful Cycle 28 HST proposal 16196 (Peterson et al. 2020). M.D., N.A., D.B., G.W., and M.Sh acknowledge support from NSF grant AST 2106249, as well as NASA STScI grants AR- 15786, AR-16600, AR-16601, and HST-AR-17556. E.M.C. gratefully acknowledges support from NASA through grant 80NSSC22 K0089. Y.H. acknowledges support from the Hubble Space Telescope program GO-16196, provided by NASA through a grant from the Space Telescope Science Institute, which is operated by the Association of Universities for Research in Astronomy, Inc., under NASA contract NAS5-26555. C.S.K. is supported by NSF grant AST-2307385. M.C.B. gratefully acknowledges support from the NSF through grant AST-2009230. H.L. acknowledges a Daphne Jackson Fellowship sponsored by the Science and Technology Facilities Council (STFC), UK. D.I., A.B.K., and L.Č.P. acknowledge funding provided by the University of Belgrade-Faculty of Mathematics (contract 451-03-66/2024-03/200104), Astronomical Observatory Belgrade (contract 451-03-66/2024-03/200002), through grants by the Ministry of Education, Science, and Technological Development of the Republic of Serbia. D.I. acknowledges the support of the Alexander von Humboldt Foundation. A.B.K. and L.Č.P. are thankful for the support by Chinese Academy of Sciences President’s International Fellowship Initiative (PIFI) for visiting scientists. A.V.F. is grateful for financial assistance from the Christopher R. Redlich Fund and numerous individual donors. M.V. gratefully acknowledges support from the Independent Research Fund Denmark via grant No. DFF 8021-00130. CSK is supported by NSF grants AST-2307385 and AST-1908570. M.R.S. is supported by the STScI Postdoctoral Fellowship. P.K. acknowledges support from NASA through the NASA Hubble Fellowship grant HST-HF2-51534.001-A awarded by the Space

Telescope Science Institute, which is operated by the Association of Universities for Research in Astronomy, Incorporated, under NASA contract NAS5-26555. J.G. gratefully acknowledges support from NASA through the grant 80NSSC22K1492. *Facility:* HST (COS, STIS).

Software: We used the Python astronomy package Astropy (Astropy Collaboration et al. 2013, 2018) for our cosmological calculations, as well as Scipy (Virtanen et al. 2020), Numpy (Harris et al. 2020), and Pandas (Reback et al. 2021) for most of our numerical computations. For our plotting purposes, we used Matplotlib (Hunter 2007).

ORCID iDs

Maryam Dehghanian  <https://orcid.org/0000-0002-0964-7500>
 Nahum Arav  <https://orcid.org/0000-0003-2991-4618>
 Gerard A. Kriss  <https://orcid.org/0000-0002-2180-8266>
 Missagh Mehdiipour  <https://orcid.org/0000-0002-4992-4664>
 Doyee Byun  <https://orcid.org/0000-0002-3687-6552>
 Gwen Walker  <https://orcid.org/0000-0001-6421-2449>
 Mayank Sharma  <https://orcid.org/0009-0001-5990-5790>
 Aaron J. Barth  <https://orcid.org/0000-0002-3026-0562>
 Misty C. Bentz  <https://orcid.org/0000-0002-2816-5398>
 Benjamin D. Boizelle  <https://orcid.org/0000-0001-6301-570X>
 Michael S. Brotherton  <https://orcid.org/0000-0002-1207-0909>
 Edward M. Cackett  <https://orcid.org/0000-0002-8294-9281>
 Elena Dalla Bontà  <https://orcid.org/0000-0001-9931-8681>
 Gisella De Rosa  <https://orcid.org/0000-0003-3242-7052>
 Gary J. Ferland  <https://orcid.org/0000-0003-4503-6333>
 Carina Fian  <https://orcid.org/0000-0002-2306-9372>
 Alexei V. Filippenko  <https://orcid.org/0000-0003-3460-0103>
 Jonathan Gelbord  <https://orcid.org/0000-0001-9092-8619>
 Michael R. Goad  <https://orcid.org/0000-0002-2908-7360>
 Keith Horne  <https://orcid.org/0000-0003-1728-0304>
 Yasaman Homayouni  <https://orcid.org/0000-0002-0957-7151>
 Dragana Ilić  <https://orcid.org/0000-0002-1134-4015>
 Michael D. Joner  <https://orcid.org/0000-0003-0634-8449>
 Erin A. Kara  <https://orcid.org/0000-0003-0172-0854>
 Shai Kaspi  <https://orcid.org/0000-0002-9925-534X>
 Christopher S. Kochanek  <https://orcid.org/0000-0001-6017-2961>
 Kirk T. Korista  <https://orcid.org/0000-0003-0944-1008>
 Peter Kosec  <https://orcid.org/0000-0003-4511-8427>
 Andjelka B. Kovačević  <https://orcid.org/0000-0001-5139-1978>
 Hermine Landt  <https://orcid.org/0000-0001-8391-6900>
 Collin Lewin  <https://orcid.org/0000-0002-8671-1190>
 Ethan R. Partington  <https://orcid.org/0000-0003-1183-1574>
 Luka Č. Popović  <https://orcid.org/0000-0003-2398-7664>
 Daniel Proga  <https://orcid.org/0000-0002-6336-5125>
 Daniele Rogantini  <https://orcid.org/0000-0002-5359-9497>
 Thaisa Storch-Bergmann  <https://orcid.org/0000-0003-1772-0023>
 Marianne Vestergaard  <https://orcid.org/0000-0001-9191-9837>
 Timothy. Waters  <https://orcid.org/0000-0002-5205-9472>
 Jian-Min Wang  <https://orcid.org/0000-0001-9449-9268>
 Fatima Zaidouni  <https://orcid.org/0000-0003-0931-0868>
 Ying Zu  <https://orcid.org/0000-0001-6966-6925>

References

- Arav, N., Becker, R. H., & Laurent-Muehleisen, S. A. 1999b, *ApJ*, 524, 566
- Arav, N., Kaastra, J., & Kriss, G. A. 2005, *ApJ*, 620, 665
- Arav, N., Edmonds, D., Borguet, B., et al. 2012, *A&A*, 544, A33
- Arav, N., Borguet, B., Chamberlain, C., et al. 2013, *MNRAS*, 436, 3286
- Arav, N., Chamberlain, C., Kriss, G. A., et al. 2015, *A&A*, 577, A37
- Arav, N., Xu, X., Kriss, G. A., et al. 2020, *A&A*, 633, A61
- Arav, N., Korista, K. T., de Kool, M., Junkkarinen, V. T., & Begelman, M. C. 1999a, *ApJ*, 516, 27
- Astropy Collaboration, Price-Whelan, A. M., Sipőcz, B. M., et al. 2018, *AJ*, 156, 123
- Astropy Collaboration, Robitaille, T. P., Tollerud, E. J., et al. 2013, *A&A*, 558, A33
- Barlow, T. A., Hamann, F., & Sargent, W. L. W. 1997, *ASPC*, 128, 13
- Bennett, C. L., Larson, D., Weiland, J. L., & Hinshaw, G. 2014, *ApJ*, 794, 135
- Bentz, M. C., & Katz, S. 2015, *PASP*, 127, 67
- Borguet, B. C. J., Edmonds, D., Arav, N., Dunn, J., & Kriss, G. A. 2012a, *ApJ*, 751, 107
- Byun, D., Arav, N., & Walker, A. 2022a, *MNRAS*, 516, 100
- Byun, D., Arav, N., & Hall, P. B. 2022b, *MNRAS*, 517, 1048
- Byun, D., Arav, N., & Hall, P. B. 2022c, *ApJ*, 927, 176
- Cackett, E. M., Gelbord, J., Barth, A. J., et al. 2023, *ApJ*, 958, 195
- Chatzikos, M., Bianchi, S., Camillioni, F., et al. 2023, *RMxAA*, 59, 327
- Chen, Z.-F., Pang, T.-T., He, b., & Huang, Y. 2018a, *ApJS*, 236, 39
- Collins, J. A., Shull, J. M., & Giroux, M. L. 2003, *ApJ*, 585, 336
- Crenshaw, D. M., & Kraemer, S. B. 2005, *ApJ*, 625, 680
- Crenshaw, D. M., Kraemer, S. B., Boggess, A., et al. 1999, *ApJ*, 516, 750
- Crenshaw, D. M., Kraemer, S. B., & George, I. M. 2003, *ARA&A*, 41, 117
- De Rosa, G., Peterson, B. M., Ely, J., et al. 2015, *ApJ*, 806, 128
- Dehghanian, M., Ferland, G. J., Kriss, G. A., et al. 2019, *ApJ*, 877, 119
- Dehghanian, M., Arav, N., Byun, D., et al. 2024, *MNRAS*, 527, 7825
- Dorodnitsyn, A., Kallman, T., & Proga, D. 2008, *ApJL*, 675, L5
- Dorodnitsyn, A., Kallman, T., & Proga, D. 2016, *ApJ*, 819, 115
- Dunn, J. P., Crenshaw, D. M., Kraemer, S. B., et al. 2008, *AJ*, 136, 1201
- Elvis, M. 2006, *MmSAI*, 77, 573
- Falco, E. E., Kurtz, M. J., Geller, M. J., et al. 1999, *PASP*, 111, 438
- Fox, A. J., Cashman, F. H., Kriss, G. A., et al. 2023, *ApJL*, 946, L48
- Gabel, J. R., Kraemer, S. B., Crenshaw, D. M., et al. 2005, *ApJ*, 631, 741
- Gaspari, M., & Sądowski, A. 2017, *ApJ*, 837, 149
- Green, J. 2009, HST Proposal, 11524
- Green, J. C., Froning, C. S., Osterman, S., et al. 2012, *ApJ*, 744, 60
- Harris, C. R., Millman, K. J., van der Walt, S. J., et al. 2020, *Natur*, 585, 357
- He, Z., Liu, G., Wang, T., et al. 2022, *SciA*, 8, eabk3291
- Homayouni, Y., De Rosa, G., Plesha, R., et al. 2023, *ApJ*, 948, 85
- Homayouni, Y., Kriss, G. A., De Rosa, G., et al. 2024, *ApJ*, 963, 123
- Hunter, J. D. 2007, *CSE*, 9, 90
- Itoh, D., Misawa, T., Horiuchi, T., & Aoki, K. 2020, *MNRAS*, 499, 3094
- Kaastra, J. S., Kriss, G. A., Cappi, M., et al. 2014, *Sci*, 345, 64
- Kallman, T., & Bautista 2001, *ApJS*, 133, 221
- Kara, E., Mehdiipour, M., Kriss, G. A., et al. 2021, *ApJ*, 922, 151
- de Kool, M., Korista, K. T., & Arav, N. 2002, *ApJ*, 580, 54
- Kriss, G. A., De Rosa, G., Ely, J., et al. 2019, *ApJ*, 881, 153
- Kriss, G. A., De Rosa, G., Barth, A. J., et al. 2022, HST Proposal, 17105
- Krolik, J. H., & Kriss, G. A. 1995, *ApJ*, 447, 512
- Krolik, J. H., & Kriss, G. A. 2001, *ApJ*, 561, 684
- Kurosawa, R., & Proga, D. 2009, *ApJ*, 693, 1929
- Longinotti, A. L., Kriss, G., Krongold, Y., et al. 2019, *ApJ*, 875, 150
- Mao, J., Kriss, G. A., Landt, H., et al. 2022, *ApJ*, 940, 41
- Mehdiipour, M., Kriss, G. A., Krongold, Y., et al. 2022, *ApJ*, 930, 166
- Miller, T. R., Arav, N., & Xu, X. 2018, *ApJ*, 865, 90
- Miller, T. R., Arav, N., Xu, X., Kriss, G. A., & Plesha, R. J. 2020c, *ApJS*, 249, 15
- Misawa, T., Charlton, J. C., Eracleous, M., et al. 2007a, *ApJS*, 171, 1
- Misawa, T., Eracleous, M., Charlton, J. C., et al. 2007b, *ASPC*, 373, 291
- Morton, D. C. 2003, *ApJS*, 149, 205
- Mościbrodzka, M., & Proga, D. 2013, *ApJ*, 767, 156
- Neustadt, J. M. M., Kochanek, C. S., Montano, J., et al. 2024, *ApJ*, 961, 219
- Noll, K. 2009, HST Proposal, 11505
- Osterbrock, D. E., & Ferland, G. J. 2006, *Astrophysics of gaseous nebulae and active galactic nuclei* (Sausalito, CA: Univ. Science Books)
- Partington, E. R., Cackett, E. M., Kara, E., et al. 2023, *ApJ*, 947, 2
- Penton, S. V., Stocke, J. T., & Shull, J. M. 2000, *ApJS*, 130, 121
- Peterson, B. M., De Rosa, G., Kriss, G. A., et al. 2020, HST Proposal, 16196
- Proga, D. 2007, *ApJ*, 661, 693

- Reback, J., McKinney, W., jbrockmendel, et al. 2021, pandas-dev/pandas: Pandas 1.2.4, v1.2.4, Zenodo, doi:[10.5281/zenodo.4681666](https://doi.org/10.5281/zenodo.4681666)
- Revalski, M., Meena, B., Martinez, F., et al. 2021, [ApJ](#), **910**, 139
- Sanfrutos, M., Longinotti, A. L., Krongold, Y., et al. 2018, [ApJ](#), **868**, 111
- Savage, B. D., & Sembach, K. R. 1991, [ApJ](#), **379**, 245
- Scannapieco, E., & Oh, S. P. 2004, [ApJ](#), **608**, 62
- Serafinelli, R., Tombesi, F., Vagnetti, F., et al. 2019, [A&A](#), **627**, A121
- Silk, J., & Rees, M. J. 1998, [A&A](#), **331**, L1
- Strauss, M. A., & Huchra, J. 1988, [AJ](#), **95**, 1602
- Tarter, C. B., Tucker, W. H., & Salpeter, E. E. 1969, [ApJ](#), **156**, 943
- Vayner, A., Wright, S. A., Murray, N., et al. 2021, [ApJ](#), **919**, 122
- Virtanen, P., Gommers, R., Oliphant, T. E., et al. 2020, [NatMe](#), **17**, 261
- Waters, T., Proga, D., Dannen, R., et al. 2017, [MNRAS](#), **467**, 3160
- Waters, T., Proga, D., & Dannen, R. 2021, [ApJ](#), **914**, 62
- Winter, L. M., Danforth, C., Vasudevan, R., et al. 2011, [ApJ](#), **728**, 28
- Xu, X., Arav, N., Miller, T., & Benn, C. 2018, [ApJ](#), **858**, 39
- Yuan, F., Yoon, D., & Li, Y.-P. 2018, [ApJ](#), **857**, 121
- Zak, M. K., Miller, J. M., Behar, E., et al. 2024, [ApJL](#), **962**, 1
- Zhi-Fu Chen, i. Q. 2013, [ApJ](#), **777**, 56